

Anomalous conductivity of two-dimensional Dirac electrons in organic conductor under pressures

Yoshikazu Suzumura* ¹ and Masao Ogata ²

¹ *Department of Physics, Nagoya University, Nagoya 464-8602, Japan*

² *Department of Physics, University of Tokyo, Bunkyo, Tokyo 113-0033, Japan*

Dirac electrons in organic conductor α -(BEDT-TTF)₂I₃ under pressures, which exhibit anomalous conductivity being nearly constant at high temperatures, have been examined using a two-dimensional tight-binding model (TB) model with both the impurity and electron-phonon (e-p) scatterings. A crucial role of scattering by acoustic phonon is shown based on the previous study for a model with simple Dirac cone [Phys. Rev. B **98**,161205 (2018)]. In addition to diagonal conductivity $\sigma_x = \sigma_{xx}$ and $\sigma_y = \sigma_{yy}$, off-diagonal conductivity σ_{xy} exists due to a tilted Dirac cone, where y (x) corresponds to a direction parallel (perpendicular) to a stacking axis of molecules. This σ_{xy} results in a rotation of axis of the principal value σ_{\pm} . Since the conductivity at high temperatures is suppressed by the e-p scattering on the Dirac cone, the increase of temperature results in a broad maximum for σ_y and a nearly constant σ_x for a moderate choice of the e-p coupling constant. Further a correlation effect is examined employing a mean-field for the on-site and nearest-neighbor-site interactions. Anisotropic behavior of σ_{ν} , ($\nu = x$ and y) is discussed by comparing with experiments of organic conductors, which present nearly constant resistivity at high temperatures.

1. Introduction

Since the discovery of two-dimensional massless Dirac fermions,¹⁾ the extensive studies have been explored in various materials. Among them, noticeable phenomena of Dirac electrons in molecular crystals,²⁾ have been studied in organic conductor α -(BEDT-TTF)₂I₃³⁾ (BEDT-TTF=bis(ethylenedithio)tetrathiafulvalene). After noting that the density of states (DOS) vanishes linearly at the Fermi energy,⁴⁾ the two-dimensional Dirac cone with a zero-gap state (ZGS)⁵⁾ was found using a tight-binding (TB) model, where transfer energies are estimated from the extended Hückel method.⁶⁾ The existence of such Dirac cone was verified by first-principles DFT calculation,⁷⁾ which has been used for studying further α -(BEDT-TTF)₂I₃ under hydrostatic pressures.⁸⁾

There are common features among organic conductors with isostructure salts,^{9,10)} α -D₂I₃ (D = ET, STF, and BETS), where ET = BEDT-TTF, STF = bis(ethylenedithio)diselenadithiafulvalene), and BETS = bis(ethylenedithio)tetraselenafulvalene. These salts display an energy band with a Dirac cone^{5,11–13)} and the resistivity at high temperatures shows nearly constant behavior,^{9,10,14–18)} while the conventional metal shows the linearly increasing one. Such unconventional behavior was also observed in Dirac electrons with nodal line semimetals of single-component molecular conductors^{19–23)} Thus, it has been believed that the nearly constant behavior in resistivity at high temperatures is attributable to the intrinsic property of the Dirac electrons.

The Dirac electrons of these organic conductors at a zero doping display ZGS, where DOS around the chemical potential increases from zero linearly. A two-band model with such ZGS shows that the static conductivity

at absolute zero temperature remains finite with a universal value, i.e., independent of the magnitude of impurity scattering owing to a quantum effect. The effect of impurity has been examined in detail by applying a self-consistent Born approximation.²⁴⁾ It is further shown that the conductivity increases with increasing the doping. The tilting of the Dirac cone, which also increases the conductivity, provides the anisotropic conductivity and the deviation of the current from the applied electric field.²⁵⁾ The conductivity at finite temperatures depends on the magnitude of the impurity scattering, Γ which is proportional to the inverse of the life time by the disorder. With increasing temperature (T), the conductivity remains unchanged for $T \ll \Gamma$, while it increases for $\Gamma \ll T$.²⁶⁾ Noting that $\Gamma \sim 0.0003$ eV for organic conductors,²⁾ a monotonous increase of the conductivity at finite temperature $T > 0.0005$ eV is expected. However the measurement of the conductivity (or resistivity) on the above organic conductor shows the almost constant behavior at high temperatures. To comprehend such an exotic phenomena, the acoustic phonon scatterings has been proposed as a possible mechanism, where a simple model of Dirac cone without tilting displays a reasonable suppression of the conductivity at high temperatures.²⁷⁾ Then, it is needed to verify that such a model with both Dirac cone and the e-p interaction quantitatively accounts for the behavior of the organic conductor.

The purpose of the present paper is to demonstrate the role of the acoustic phonon in α -(BEDT-TTF)₂I₃, which gives rise to anomalous conductivity being nearly constant at high temperatures. We clarify characteristics of Dirac electrons with large tilting,^{28–30)} where transfer energies between molecules are estimated from the X-ray diffraction experiment and DFT. A TB model with transfer energies of α -(BEDT-TTF)₂I₃ under pressures is

*E-mail: suzumura@s.phys.nagoya-u.ac.jp

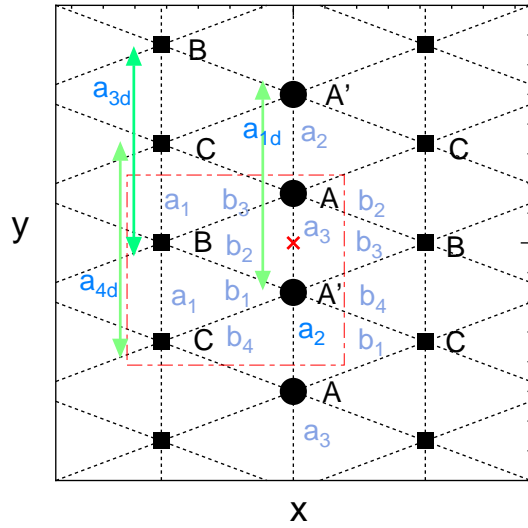


Fig. 1. (Color online) Crystal structure, where there are four molecules A, A', B and C in the unit cell (dot-dashed line), which forms a square lattice. Transfer energies are shown by a_1, \dots, b_4 for the nearest neighbor (NN) sites and a_{1d}, a_{3d} , and a_{4d} for the next-nearest neighbor (NNN) sites.

examined, which are well known compared with those of other isostructural salts, BETS and STF. Since the tilted Dirac cone is also obtained for BETS¹²⁾ and STF,¹³⁾ it is expected that the present TB model provides a common feature for these salts, i.e., the nearly constant conductivity at high temperatures.

The paper is organized as follows. In Sect. 2, model and formulation are given for both the uniaxial and hydrostatic pressure, where the latter case is examined by adding site potential due to interaction. In Sect. 3, after examining the chemical potential and density of states (DOS), the conductivity is calculated for α -(BEDT-TTF)₂I₃ under both uniaxial and hydrostatic pressures. Sect. 4 is devoted to summary and discussion.

2. Model and Formulation

We consider a two-dimensional system per spin, which is given by,

$$H_{\text{total}} = H_0 + H_1 + H_p + H_{e-p} + H_{\text{imp}}. \quad (1)$$

H_0 describes a TB model of organic conductor α -(BEDT-TTF)₂I₃ consisting of four molecules per unit cell (Fig. 1). H_1 describes a site potential, which is obtained from a mean field of short range repulsive interactions. H_p and H_{e-p} denote an acoustic phonon and an electron-phonon (e-p) interaction. H_{imp} is the impurity potential. The terms $H_0 + H_p + H_{e-p}$ are the Fröhlich Hamiltonian³¹⁾ applied to the present Dirac electron system. The unit of the energy is taken as eV.

2.1 Energy band

First, we derive the energy band for $H = H_0 + H_1$ and the associated quantities. A TB model, H_0 , is expressed

as

$$\begin{aligned} H_0 &= \sum_{i,j=1}^N \sum_{\alpha,\beta=1}^4 t_{i,j;\alpha,\beta} a_{i,\alpha}^\dagger a_{j,\beta} \\ &= \sum_{\mathbf{k}} \sum_{\alpha,\beta=1}^4 t_{\alpha,\beta}(\mathbf{k}) a_\alpha^\dagger(\mathbf{k}) a_\beta(\mathbf{k}), \end{aligned} \quad (2)$$

where $a_{i,\alpha}^\dagger$ denotes a creation operator of an electron of molecule α [A(1), A'(2), B(3), and C(4) in the unit cell at the i -th lattice site. N is a total number of the square lattice sites and $t_{i,j;\alpha,\beta}$ are the transfer energies for the nearest and next-nearest neighbor sites, which are shown in Fig. 1. A Fourier transform for the operator $a_{j,\alpha}$ is given by $a_{j,\alpha} = 1/N^{1/2} \sum_{\mathbf{k}} a_\alpha(\mathbf{k}) \exp[i\mathbf{k} \cdot \mathbf{r}_j]$, where $\mathbf{k} = (k_x, k_y)$ and the lattice constant is taken as unity. The quantity H_1 corresponds to a site potential, V_α , acting on the α site, where $V_A = V_{A'}$ due to an inversion symmetry around the cross in Fig. 1. The Hamiltonian H_1 is obtained as

$$\begin{aligned} H_1 &= \sum_{\alpha} (V_\alpha - V_A) \hat{n}_\alpha \\ &= \tilde{V}_B \hat{n}_B + \tilde{V}_C \hat{n}_C, \end{aligned} \quad (3)$$

where \tilde{V}_α denotes a potential measured from that of the A site and $\hat{n}_\alpha = a_\alpha^\dagger(\mathbf{k}) a_\alpha(\mathbf{k})$. From Eqs. (2) and (3), H is written as

$$H = \sum_{\mathbf{k}} \sum_{\alpha,\beta} a_\alpha^\dagger(\mathbf{k}) h_{\alpha,\beta} a_\beta(\mathbf{k}), \quad (4)$$

where matrix elements, $h_{\alpha,\beta}$, are given as follows.

$$h_{12}(\mathbf{k}) = a_3 + a_2 Y, \quad (5a)$$

$$h_{13}(\mathbf{k}) = b_3 + b_2 X, \quad (5b)$$

$$h_{14}(\mathbf{k}) = b_4 Y + b_1 X Y, \quad (5c)$$

$$h_{23}(\mathbf{k}) = b_2 + b_3 X, \quad (5d)$$

$$h_{24}(\mathbf{k}) = b_1 + b_4 X, \quad (5e)$$

$$h_{34}(\mathbf{k}) = 2a_1, \quad (5f)$$

$$h_{11}(\mathbf{k}) = t_{22}(\mathbf{k}) = a_{1d}(Y + \bar{Y}), \quad (5g)$$

$$h_{33}(\mathbf{k}) = a_{3d}(Y + \bar{Y}) + \tilde{V}_B, \quad (5h)$$

$$h_{44}(\mathbf{k}) = a_{4d}(Y + \bar{Y}) + \tilde{V}_C, \quad (5i)$$

and $h_{ij}(\mathbf{k}) = h_{ji}^*(\mathbf{k})$, where $X = \exp[ik_x] = \bar{X}^*$ and $Y = \exp[ik_y] = \bar{Y}^*$. The matrix elements of H_1 are \tilde{V}_B for $\alpha = \beta = 3$, \tilde{V}_C for $\alpha = \beta = 4$ and zero otherwise. Equation (4) is diagonalized as

$$H = \sum_{\mathbf{k}} \sum_{\gamma} c_\gamma^\dagger(\mathbf{k}) E_\gamma(\mathbf{k}) c_\gamma(\mathbf{k}), \quad (6a)$$

where $E_1(\mathbf{k}) > E_2(\mathbf{k}) > E_3(\mathbf{k}) > E_4(\mathbf{k})$ and

$$c_\gamma(\mathbf{k}) = \sum_{\alpha} d_{\alpha\gamma}(\mathbf{k}) a_\alpha(\mathbf{k}). \quad (6b)$$

The Dirac point (\mathbf{k}_D) is obtained from

$$E_1(\mathbf{k}_D) = E_2(\mathbf{k}_D) = \epsilon_D. \quad (7)$$

The ZGS is obtained when ϵ_D becomes equal to the chemical potential at $T=0$.

In the present paper, the site potentials \tilde{V}_B and \tilde{V}_C in H_1 are given by the mean-field of short-range repulsive interactions,⁸⁾

$$\begin{aligned} \tilde{V}_B &= (n_B - n_A)U/2 \\ &+ 2V_a(n_C - n_A) + 2V_b(2n_A - n_B - n_C), \end{aligned} \quad (8a)$$

$$\begin{aligned} \tilde{V}_C &= (n_C - n_A)U/2 \\ &+ 2V_a(n_B - n_A) + 2V_b(2n_A - n_B - n_C). \end{aligned} \quad (8b)$$

where U is the on-site repulsive interaction and V_a (V_b) denotes the nearest neighbour interaction along the y (x) axis. n_α denotes a local density corresponding to an electron number per unit cell at the α site. From E_γ , n_α including both spin \uparrow and \downarrow is calculated as

$$\begin{aligned} n_\alpha &= \frac{2}{N} \sum_{\mathbf{k}} \langle \hat{n}_\alpha(\mathbf{k}) \rangle_H \\ &= \frac{2}{N} \sum_{\mathbf{k}} \sum_{\gamma} d_{\alpha\gamma}^*(\mathbf{k}) d_{\alpha\gamma}(\mathbf{k}) f(E_\gamma(\mathbf{k}) - \mu), \end{aligned} \quad (9)$$

which is determined self-consistently. $n_A = n_{A'}$ due to transfer energies being symmetric with respect to the inversion center between A and A' in Fig. 1. In Eq. (9), $f(\epsilon) = 1/(\exp[\epsilon/T] + 1)$ with T being temperature in the unit of eV and $k_B = 1$. The chemical potential μ is determined from the three-quarter-filled condition, which is given by

$$\frac{1}{N} \sum_{\mathbf{k}} \sum_{\gamma} f(E_\gamma(\mathbf{k}) - \mu) = \int_{-\infty}^{\infty} d\omega D(\omega) f(\omega) = 3, \quad (10)$$

where

$$D(\omega) = \frac{1}{N} \sum_{\mathbf{k}} \sum_{\gamma} \delta(\omega - E_\gamma(\mathbf{k})). \quad (11)$$

$D(\omega)$ denotes DOS per spin and per unit cell, which satisfies $\int d\omega D(\omega) = 4$. Note that $n_A + n_{A'} + n_B + n_C = 6$ from Eq. (10). We use $\mu(T)$ at finite T and $\mu = \mu(0)$ at $T=0$.

2.2 Scattering by phonon and impurity

In Eq. (1), the third term denotes the harmonic phonon given by $H_p = \sum_{\mathbf{q}} \omega_{\mathbf{q}} b_{\mathbf{q}}^\dagger b_{\mathbf{q}}$ with $\omega_{\mathbf{q}} = v_s |\mathbf{q}|$ and $\hbar = 1$, while the fourth term is the e-p interaction expressed as³¹⁾

$$H_{e-p} = \sum_{\mathbf{k}, \gamma} \sum_{\mathbf{q}} \alpha_{\mathbf{q}} c_\gamma(\mathbf{k} + \mathbf{q})^\dagger c_\gamma(\mathbf{k}) \phi_{\mathbf{q}}, \quad (12)$$

with $\phi_{\mathbf{q}} = b_{\mathbf{q}} + b_{-\mathbf{q}}^\dagger$. We introduce a coupling constant $\lambda = |\alpha_{\mathbf{q}}|^2 / \omega_{\mathbf{q}}$ which becomes independent of $|\mathbf{q}|$ for small $|\mathbf{q}|$. The e-p scattering is considered within the same band (i.e., intraband) due to the energy conservation with $v \gg v_s$, where $v \simeq 0.05^8)$ denotes the averaged velocity of Dirac cone. The last term of Eq. (1), H_{imp} denotes a normal impurity scattering, which is introduced to obtain the finite conductivity and to avoid the infinite conductivity in the presence of only the e-p interaction.³²⁾

Noting that the band is three-quarter filled owing to 2:1 salt, we calculate an energy difference defined by

$$\Delta(\mathbf{k}) = E_1(\mathbf{k}) - E_2(\mathbf{k}), \quad (13)$$

where the Dirac point \mathbf{k}_D is obtained from $\Delta(\mathbf{k}_D) = 0$ as shown in the next section. Since $E_\gamma(\mathbf{k}_D) = \mu$ ($\gamma = 1, 2$) for the present ZGS, the low temperature property is determined from $|E_\gamma(\mathbf{k}) - \mu| \ll T$.

The damping of the electron of the γ band, which is defined by Γ_γ , is obtained from the electron Green function³³⁾ expressed as,

$$G_\gamma(\mathbf{k}, i\omega_n)^{-1} = i\omega_n - E_{\gamma, \mathbf{k}} + \mu + i\Gamma_\gamma, \quad (14a)$$

$$\Gamma_\gamma = \Gamma + \Gamma_{\text{ph}}^\gamma, \quad (14b)$$

where $\Gamma_{\text{ph}}^\gamma = -\text{Im}\Sigma_\gamma(\mathbf{k}, E_{\gamma, \mathbf{k}} - \mu)$ with $\Sigma_\gamma(\mathbf{k}, E_{\gamma, \mathbf{k}} - \mu)$ being a self-energy by the e-p interaction. The real part of the self-energy can be neglected for small doping.²⁷⁾ The quantity Γ comes from another self-energy by the impurity scattering. Note that $\Gamma_{\text{ph}}^\gamma$ does not depend on Γ , and that the ratio $\Gamma_{\text{ph}}^\gamma/\Gamma$ is crucial to determine the T dependence of the conductivity. The quantity $\Sigma_\gamma(\mathbf{k}, \omega) = \Sigma_\gamma(\mathbf{k}, i\omega_n)$ with $i\omega_n \rightarrow \omega + 0$ is estimated as³³⁾

$$\begin{aligned} \Sigma_\gamma(\mathbf{k}, i\omega_n) &= T \sum_m \sum_{\mathbf{q}} |\alpha_{\mathbf{q}}|^2 \\ &\times \frac{1}{i\omega_{n+m} - \xi_{\gamma, \mathbf{k}+\mathbf{q}}} \times \frac{2\omega_{\mathbf{q}}}{\omega_m^2 + \omega_{\mathbf{q}}^2}, \end{aligned} \quad (15)$$

which is a product of electron and phonon Green functions. $\omega_n = (2n+1)\pi T$, $\omega_m = 2\pi mT$ with n and m being integers. $\xi_{\gamma, \mathbf{k}} = E_{\gamma, \mathbf{k}} - \mu$. Applying the previous result,²⁷⁾ we obtain

$$\Gamma_{\text{ph}}^\gamma = C_0 R \times T |\xi_{\gamma, \mathbf{k}}|, \quad (16a)$$

$$R = \frac{\lambda}{\lambda_0}, \quad (16b)$$

where $C_0 = 6.25\lambda_0/(2\pi v^2)$. For $v \simeq 0.05$ and $\lambda_0/2\pi v = 0.1$, we obtain $C_0 \simeq 12.5$ (eV)⁻¹. R denotes a normalized e-p coupling constant.

Using the component of the wave function $d_{\alpha\gamma}$ in Eq. (6b), the response function per spin and per site is calculated by³⁴⁾

$$\begin{aligned} \sigma_{\nu\nu'}(T) &= \frac{e^2}{\pi\hbar N} \sum_{\mathbf{k}} \sum_{\gamma, \gamma'} v_{\gamma\gamma'}^\nu(\mathbf{k})^* v_{\gamma\gamma'}^{\nu'}(\mathbf{k}) \\ &\int_{-\infty}^{\infty} d\epsilon \left(-\frac{\partial f(\epsilon)}{\partial \epsilon} \right) \\ &\times \frac{\Gamma_\gamma}{(\epsilon - \xi_{\mathbf{k}\gamma})^2 + \Gamma_\gamma^2} \times \frac{\Gamma_{\gamma'}}{(\epsilon - \xi_{\mathbf{k}\gamma'})^2 + \Gamma_{\gamma'}^2}, \end{aligned} \quad (17)$$

$$v_{\gamma\gamma'}^\nu(\mathbf{k}) = \sum_{\alpha\beta} d_{\alpha\gamma}(\mathbf{k})^* \frac{\partial \tilde{H}_{\alpha\beta}}{\partial k_\nu} d_{\beta\gamma'}(\mathbf{k}), \quad (18)$$

where $\nu = x$ and y . $h = 2\pi\hbar$ and e denote a Plank's constant and electric charge, respectively.

In terms of $\sigma_{xx} = \sigma_x = A$, $\sigma_{yy} = \sigma_y = B$, and $\sigma_{xy} = C$, the current (j_x, j_y) obtained from a response to an

external electric field (E_x, E_y) is written as

$$\begin{pmatrix} j_x \\ j_y \end{pmatrix} = \begin{pmatrix} A & C \\ C & B \end{pmatrix} \begin{pmatrix} E_x \\ E_y \end{pmatrix}. \quad (19)$$

The principal axis of Dirac cone has an angle ϕ measured from the k_y axis, where $-\pi/2 < \phi < \pi/2$. When we denote the current and the electric field in this axis direction as j'_x and E'_x , we obtain

$$\begin{pmatrix} j'_x \\ j'_y \end{pmatrix} = \begin{pmatrix} \sigma_1 & 0 \\ 0 & \sigma_2 \end{pmatrix} \begin{pmatrix} E'_x \\ E'_y \end{pmatrix}, \quad (20a)$$

where

$$\begin{pmatrix} j'_x \\ j'_y \end{pmatrix} = \begin{pmatrix} \cos \phi & \sin \phi \\ -\sin \phi & \cos \phi \end{pmatrix} \begin{pmatrix} j_x \\ j_y \end{pmatrix}, \quad (20b)$$

$$\begin{pmatrix} E'_x \\ E'_y \end{pmatrix} = \begin{pmatrix} \cos \phi & \sin \phi \\ -\sin \phi & \cos \phi \end{pmatrix} \begin{pmatrix} E_x \\ E_y \end{pmatrix}. \quad (20c)$$

The relations between $(\sigma_1, \sigma_2, \phi)$ and (A, B, C) are

$$\tan 2\phi = \frac{2C}{A-B}, \quad (21a)$$

$$\sigma_1 = \sigma_- = \frac{1}{2}[A+B - \sqrt{(A-B)^2 + 4C^2}], \quad (21b)$$

$$\sigma_2 = \sigma_+ = \frac{1}{2}[A+B + \sqrt{(A-B)^2 + 4C^2}]. \quad (21c)$$

Note that $\phi < 0$ for $C > 0$ and $\phi > 0$ for $C < 0$, where $0 < |\phi| < \pi/4$ for $B > A$ and $\pi/4 < |\phi| < \pi/2$ for $A > B$.

It is noted that Eq. (17) can be understood using DOS when \mathbf{k} dependence of $v'_{\gamma,\gamma}$ close to the Dirac point is small. In fact, as shown in the next section, with increasing temperature the conductivity in the absence of the e-p interaction increases monotonously due to the increase of DOS since the chemical potential moves away from that of the Dirac point.²⁵⁾

3. Conductivity of Dirac electrons

We calculate the conductivity for the TB model with transfer energies shown in Fig. 1. The direction of molecular stacking is given by the y axis, while that perpendicular to the stacking is given by the x axis. The nearest neighbour (NN) transfer energies are examined for both uniaxial pressure and hydrostatic pressure, while those of next nearest neighbor (NNN) sites are added only for hydrostatic pressure.⁷⁾ In the following calculations, the conductivity is normalized by e^2/\hbar and the energy is scaled by eV. First we examine the case of uniaxial pressure ($P = 6$) without site potential, and study next a case of hydrostatic pressure with site potential to comprehend the similarity and dissimilarity.

3.1 α -(BEDT-TTF)₂I₃ under uniaxial pressures

The TB model under uniaxial pressure P is calculated using nearest neighbor transfer energies at P kbar, which are given by $a_1 = -0.028(1 + 0.089P)$, $a_2 = -0.048(1 + 0.167P)$, $a_3 = 0.02(1 - 0.025P)$, $b_1 = 0.123$,

$b_2 = 0.140(1 + 0.011P)$, $b_3 = 0.062(10.032P)$, and $b_4 = 0.025$.⁵⁾

There are following characteristics in the band structure. Figure 2(a) shows the ZGS at $P = 6$ kbar, where $E_1(\mathbf{k})$ and $E_2(\mathbf{k})$ touch at the Dirac points $\mathbf{k}_D = \pm(0.57, 0.30)\pi$ with an energy $\epsilon_D = \mu = 0.178$ due to three-quarter-filled band. In fact, energies of the conduction and valence bands $E_1(\mathbf{k})$ and $E_2(\mathbf{k})$ exist for $0 < E_1(\mathbf{k}) - \mu < 0.19$ and $-0.11 < E_2(\mathbf{k}) - \mu < 0$, respectively. Such ZGS shows a relation $E_2(Y) < \epsilon_D < E_1(X) < E_1(M)$, where Y, X and M are TRIMs given by $\Gamma = (0, 0)\pi$, $X = (1, 0)\pi$, $Y = (0, 1)\pi$, and $M = (1, 1)\pi$. Note that, for $P = 4$ and 8 , $\mu = 0.172$, and 0.185 and $\mathbf{k}_D = \pm(0.6, 0.35)\pi$ and $\pm(0.55, 0.25)\pi$, respectively. Figure 2(b) shows contour plots of $E_1(\mathbf{k}) - E_2(\mathbf{k})$, as the function of $\delta\mathbf{k} = \mathbf{k} - \mathbf{k}_D$ in a small region around \mathbf{k}_D . The line surrounding the orange region given by $E_1(\mathbf{k}) - E_2(\mathbf{k}) < 0.03$, is almost a circle suggesting that the velocity of the Dirac cone is isotropic. Figure 2(c) shows $E_1(\mathbf{k}) - \epsilon_D$. The Dirac point is located at the darkest region, where the ellipse for the fixed $E_1(\mathbf{k}) - \epsilon_D$ suggests a tilted Dirac cone. Note that the axis of the cone shows slight rotation clockwise from the k_x axis, which plays a crucial role for the transport property as shown later. Figure 2(d) shows $E_2(\mathbf{k}) - \epsilon_D$. The Dirac point is located at the brightest region, where the ellipse for the fixed $E_2(\mathbf{k}) - \epsilon_D$ also suggests a tilted Dirac cone. We define a phase $\phi_1 (< 0)$ (ϕ_2) as a tilting angle of $E_1(\mathbf{k})$ ($E_2(\mathbf{k})$) measured from the k_x axis. Since $E_1(\mathbf{k})$ and $E_2(\mathbf{k})$ form a pair of Dirac cone, $\phi_2 - \phi_1 = \pi$ for \mathbf{k} in the limit of the Dirac point. The deviation from the limiting value increases with increasing $|\delta\mathbf{k}_D|$. The tilting parameter is given by $\eta \sim 0.8$.

Figure 3 shows the temperature (T) dependence of the chemical potential ($\mu(T)$) at $P = 6$ (solid line) and a hydrostatic pressure P_{hydro} (dashed line), where the corresponding DOS as a function of $\omega - \mu$ is shown in the inset. With increasing T , μ varies slowly suggesting that the T dependence of μ on σ_ν is negligibly small. In fact, the T dependence of μ in Eq. (16a) may be ignored for $\sigma_\nu(T)$ at low temperatures. We verified that $\mu(T)$ can be replaced by $\mu(0)$ in $\xi_{\gamma,\mathbf{k}}$ for $0 < T < 0.015$ ($0 < T < 0.013$) which is the range of temperature of the following numerical calculation of σ_ν under the pressure of $P=6$ kbar (P_{hydro}). The DOS close to the chemical potential shows a linear dependence with respect to $\omega - \mu$, where μ is the chemical potential at $T=0$. The slight decrease of the chemical potential at low temperatures comes from the peak above the chemical potential corresponding to the van hove singularity at $E_1(X)$ in DOS. The increase of μ above the minimum occurs since the van hove singularity at $E_2(Y)$ below the chemical potential has a large peak compared with that of $E_1(X)$. Similar behavior is found for P_{hydro} , which shows the increase of the band width.

Figure 4 shows the temperature dependence of conductivity of σ_ν ($\nu = x, y, xy, +, -$) without the e-p interaction, where $P = 6$ and $\Gamma = 0.0005$. For another choice of $\Gamma = 0.001$, σ_y and σ_\pm becomes smaller, while σ_x is smaller for $T > 0.011$ and σ_x is larger for

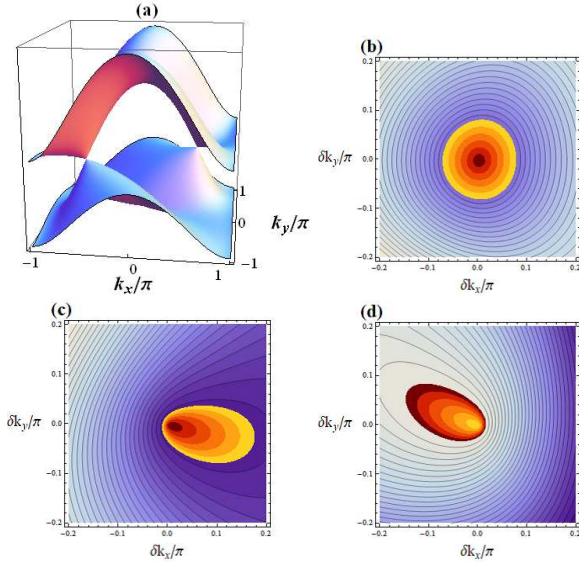


Fig. 2. (Color online) (a) Conduction and valence bands given by $E_1(\mathbf{k})$ (upper band) and $E_2(\mathbf{k})$ (lower band) at $P=6$ kbar. Two bands contact at the Dirac points $\mathbf{k}_D = \pm(0.57, 0.30)\pi$ with an energy $\epsilon_D = \mu = 0.178$. (b) Contour plots of $E_1(\mathbf{k}) - E_2(\mathbf{k})$, where $\delta\mathbf{k} (= \mathbf{k} - \mathbf{k}_D)$. The Dirac point, $\mathbf{k}_D = (0.57, 0.30)\pi$, is obtained in the middle of the orange region given by $E_1(\mathbf{k}) - E_2(\mathbf{k}) < 0.03$. (c) Contour plots of $E_1(\mathbf{k}) - \epsilon_D$, where the Dirac point exists at a bottom of the orange region given by $0 < E_1(\mathbf{k}) - \epsilon_D < 0.005$. (d) Contour plots of $E_2(\mathbf{k}) - \epsilon_D$. The Dirac point exists at the top of the orange region given by $-0.005 < E_2(\mathbf{k}) - \epsilon_D < 0$.

$T < 0.011$. The conductivity in the zero limit of T is given by $\sigma_x(0) \simeq 0.06$ and $\sigma_y(0) \simeq 0.09$, respectively which are compared with that of the universal value of $1/2\pi^2 = 0.051$. The slightly larger value in the present case comes from the tilting of the Dirac cone.²⁵⁾ At low temperatures, we obtain an equality $\sigma_y > \sigma_x$, which can be understood as follows. Figure 2(b) shows a nearly isotropic velocity of the Dirac cone, while Figs. 2(c) and 2(d) present a large tilting of the Dirac cone along the k_x direction. Our previous calculation of a tilted Dirac cone shows that the conductivity becomes maximum for the direction perpendicular to a tilting axis.²⁵⁾ Thus we obtain $\sigma_y > \sigma_x$ at low temperature in the present case. Compared with such inequality at low temperatures, an opposite relation of $\sigma_x > \sigma_y$ is found for $T > 0.012$. The transport at high temperatures is determined by electrons with higher energy, where the transfer energy along the x direction is larger than that of y direction. Such crossover occurs at lower T for larger Γ . This is compatible with a fact that the reduction of σ_y by Γ is larger than that of σ_x . We also note that such crossover occurs at higher T for $P=8$ (not shown here).

The dashed line in Fig. 4 shows the T dependence of the principal value σ_{\pm} . In the limit of $T=0$, we obtain $\sigma_+(0) \simeq 0.092$ and $\sigma_-(0) \simeq 0.067$, which give $\sigma_+(0)/\sigma_0 \simeq 1.82$ and $\sigma_-(0)/\sigma_0 \simeq 1.32$ with $\sigma_0 = 1/(2\pi^2)$. These results are compatible with the analytical results of tilted Dirac cone where $\sigma_+/\sigma_0 = 1.84$ and $\sigma_-/\sigma_0 = 1.19$ for $\eta = 084$.²⁵⁾ The behavior of σ_{\pm} being linear in T resembles that of DOS around $\omega = \mu$ in the

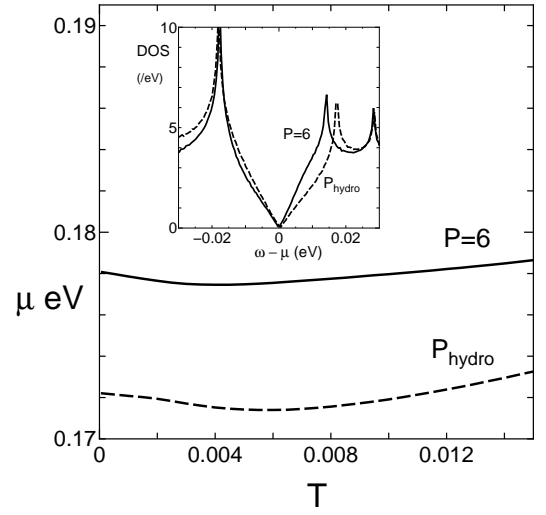


Fig. 3. Chemical potential (μ) as a function of temperature (T) for $P=6$ (solid line) and $P=P_{\text{hydro}}$ (dashed line). It is found that $\mu(T)$ for $P=6$ ($P=P_{\text{hydro}}$) takes a minimum at $T \sim 0.004$ ($T \sim 0.006$). The inset denotes the corresponding DOS as a function of $\omega - \mu$ with $\mu(T=0)$ is given by 0.178 for $P=6$ and 0.172 for $P=P_{\text{hydro}}$.

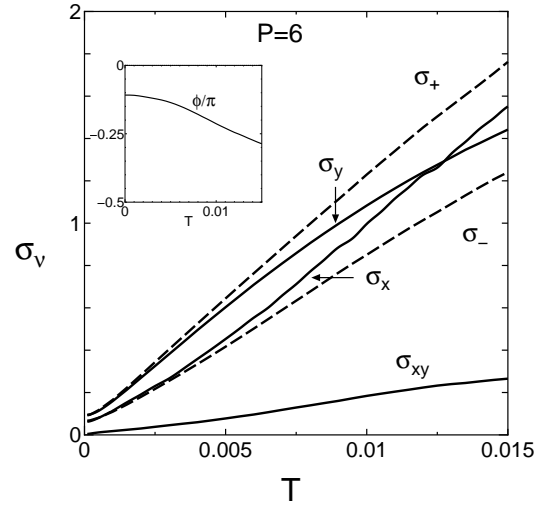


Fig. 4. T dependence of conductivity in the absence of the e-p interaction at $P=6$ with fixed $\Gamma = 0.0005$, where the solid line denotes σ_x , σ_y and σ_{xy} and dashed line denotes σ_{\pm} . Principal values of σ_- and σ_+ are given by Eqs. (21b) and (21c) while ϕ is given by Eq. (21a). The inset shows the phase ϕ , which is an angle of the principal axis of σ_- measured from the k_x axis.

inset of Fig. 3, which is found for $|\omega - \mu| < 0.015$. The inset displays T dependence of ϕ , where $\phi < 0$ due to $\sigma_{xy} > 0$ and $\sigma_y > \sigma_x$ at low temperatures as seen from Eq. (21a). With increasing T , ϕ decreases and becomes smaller than $-\pi/4$ at a temperature corresponding to $\sigma_x = \sigma_y$, where the axis close to σ_- changes from k_x axis to the k_y axis. Thus the principal axes rotates clockwise with an angle $\phi (< 0)$ (see Eq. (20c)).

As shown in Fig. 4 ($P=6$), σ_{ν} increases monotonously as the function of T , which is different from the experiment showing nearly constant behavior at high temper-

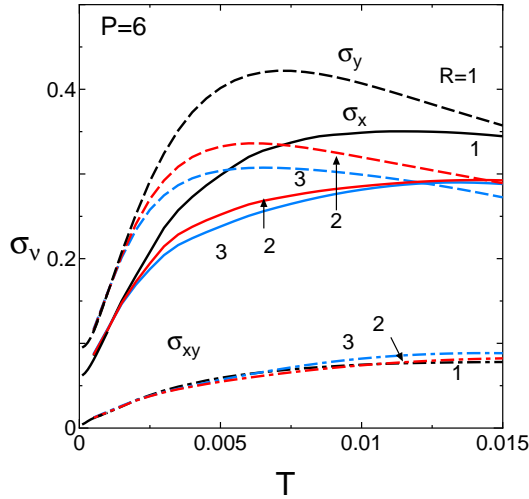


Fig. 5. (Color online) Conductivity σ_ν ($\nu = x, y$, and xy) in the presence of the e-p interaction with $P = 6$ and $\Gamma = 0.0005$. The solid line, dashed line and dot-dashed line denote σ_x , σ_y , and σ_{xy} , respectively, where R denotes a normalized e-p coupling constant defined by a ratio of λ/λ_0 (Eq. (16b)). $R = 1$ corresponds to $\lambda = 0.1$. At high T , σ_x shows almost constant behavior and σ_y shows a broad maximum.

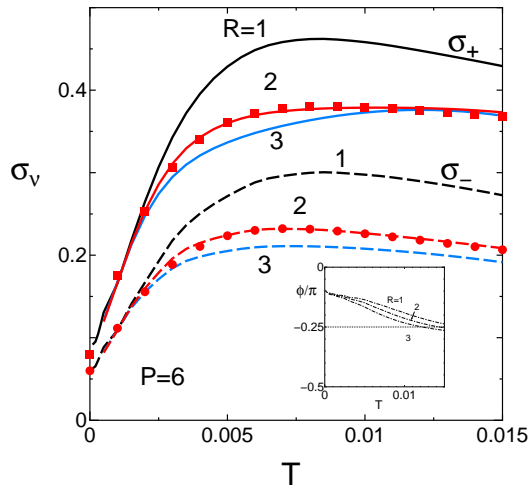


Fig. 6. (Color online) Conductivity σ_\pm with $P = 6$ and $\Gamma = 0.0005$ in the presence of the e-p interaction. The solid line and the dashed line correspond to σ_+ and σ_- , which show a broad maximum. The symbols are obtained by fitting to the respective lines. The inset denotes the corresponding ϕ .

atures.²⁾ Such exotic T dependence of σ_ν is examined next by taking account of the e-p interaction, which is expected to reduce σ_ν . Using Eq. (14b) and (16a), σ_ν of Eq. (17) is calculated, where Γ in the absence of the e-p interaction is replaced by $\Gamma_\gamma (= \Gamma + \Gamma_{\text{ph}}^\gamma)$. Owing to the T dependence of $\Gamma_{\text{ph}}^\gamma$, Γ is dominant at low T while $\Gamma_{\text{ph}}^\gamma$ is dominant at high T . Note that such crossover with increasing T depends on R .

Figure 5 shows the T dependence of σ_ν ($\nu = x, y, xy$) in the presence of the e-p interaction with some choices of R . Compared with σ_ν with $R = 0$ (Fig. 4), σ_ν with $R \neq 0$ is reduced noticeably. At temperatures around

$T \sim 0.015$, σ_x is nearly constant, while σ_y takes a broad maximum at lower temperatures. Noting that the difference in σ_x and σ_y at low temperatures is noticeably reduced at high temperatures, it is found that the tilting effect of the Dirac cone in the presence of moderate strength of R varies with increasing temperatures. The R dependence on σ_{xy} is small. The crossover temperature corresponding to $\sigma_x = \sigma_y$ decreases with increasing R , since the reduction of σ_y is larger than that of σ_x . The nearly constant behavior of σ_x is understood as follows. In the absence of the e-p interaction, σ_ν as a function of T increases linearly, which comes from DOS determined by the Dirac cone. However for $R \neq 0$, the noticeable effect of the acoustic phonon emerges at finite temperatures. As shown in Eq. (14b), the electron is scattered by both normal impurity (Γ) and the e-p interaction ($\Gamma_{\text{ph}}^\gamma$), where the increase of the latter at finite temperature is seen from Eq. (16a). However, compared with the conventional metal with a Fermi surface, where the increase of temperature gives rise to a large enhancement of the e-p scattering to suppress the conductivity, the effect of the e-p scattering in the case of the Dirac cone close to the three-quarter-filled band is strongly reduced due to a constraint by the energy-momentum conservation.²⁷⁾ Thus, we obtain nearly constant behavior or a broad maximum in σ_ν , due to a competition between the enhancement by DOS of the Dirac cone and the suppression by the e-p interaction.

Figure 6 shows the T dependence of the principal values σ_\pm corresponding to Fig. 5. Since σ_+ and σ_- give the upper and lower bound of the conductivity, these quantities are convenient to comprehend experiments even when the exact correspondence between the crystal axis and the direction of the applied electric field is not known. In the inset, the rotation angle is shown, where $\phi < 0$ for $\sigma_{xy} > 0$ and $\sigma_y > \sigma_x$. The angle $|\phi|$ increases and exceeds $\pi/4$ at a certain temperature ($\sigma_x = \sigma_y$), implying that the axis of σ_- becomes closer to k_y -axis at high temperatures. Since σ_+ and σ_- have a common feature of a broad maximum with increasing T , we examine the origin of such maximum of σ_ν by using a numerical fitting of σ_\pm . We apply a fitting formula given by

$$\sigma_\nu = \sigma_{0,\nu} + \frac{a_\nu 10^3 T}{1 + b_\nu 10^6 T^2 / (1 + c_\nu 10^3 T)}, \quad (22a)$$

which is shown by symbols for $R=2$ in Fig. 6. Fitting parameters a_ν , b_ν , and c_ν in Eq. (22a) are obtained as follows. First, σ_ν in the absence of the e-p interaction is fitted by $\sigma_{0,\nu}$ and a_ν . Next, the T dependence around a maximum is fitted by b_ν and c_ν . These coefficients are estimated as $\sigma_{0,+} = 0.08$, $a_+ = 0.1$, $b_+ = 0.046$, $c_+ = 0.1$ and $\sigma_{0,-} = 0.06$, $a_- = 0.053$, $b_- = 0.028$, $c_- = 0.031$ for $R=2$. Such a formula can be derived based on a simplified model,²⁷⁾ where $\sigma_+ \sim \sigma_- \sim \sigma$. Note that $\Gamma_{\text{ph}}^\gamma$ is obtained in Eq. (16a) and $\sigma \simeq a'_\nu 10^3 T / \Gamma$ with $a'_\nu = o(0.1)$ without e-p interaction. Taking Γ replaced by $\Gamma + \Gamma_{\text{ph}}^\gamma$ and employing an idea $|\langle \xi_{\gamma,\mathbf{k}} \rangle| \sim T$ with $\langle \rangle$ being an average value in the summation of Eq. (15),

we obtain

$$\sigma \simeq \frac{a'_\nu 10^3 T}{1 + C_0 R T^2 / \Gamma}, \quad (22b)$$

with $C_0 = 12.5$ and $\Gamma = 0.0005$. Both equations Eqs. (22a) and (22b) are compatible due to $C_0 R T^2 / \Gamma \simeq b_\nu 10^6 T^2$ with $R = 2$. From Eq. (22b), it is found that a maximum of σ as a function of T is obtained by a competition between the increase of DOS (the enumerator) and the suppression the denominator by the e-p interaction of competition. Equation (22b) suggests that σ decreases with increasing R .

3.2 α -(BEDT-TTF) $_2$ I $_3$ under hydrostatic pressures

We examine Dirac electrons under hydrostatic pressure using the TB model with NN (a_1, \dots, b_4) and NNN (a_{1d}, \dots, a_{4d}) transfer energies, which are given by⁷⁾ $a_1 = -0.0267$, $a_2 = -0.0511$, $a_3 = 0.0323$, $b_1 = 0.1241$, $b_2 = 0.1296$, $b_3 = 0.0513$, $b_4 = 0.0152$, $a_{1d} = 0.0119$, $a_{3d} = 0.0046$, and $a_{4d} = 0.0060$. We use the site potentials given by Eqs. (8a) and (8b).⁸⁾ They are estimated as $\tilde{V}_B = 0.0511$, $\tilde{V}_C = 0.0032$ for $U = 0.4$, $V_a = 0.17$, and $V_b = 0.05$, where $n_A = n_{A'} = 1.46$, $n_B = 1.37$, and $n_C = 1.71$, and $\mu = 0.172$ at $T = 0$.

Band energies $E_j(\mathbf{k})$ under hydrostatic pressure, which have Dirac cones similar to Fig. 2, show the following difference. Figure 7(a) shows the conduction and valence bands ($0 < E_1(\mathbf{k}) - \mu < 0.15$ and $-0.09 < E_2(\mathbf{k}) - \mu < 0$) in the first Brillouin zone, which touch at the Dirac points $\mathbf{k}_D = \pm(0.69, 0.44)\pi$. Compared with Fig. 2(a), the band width of both $E_1(\mathbf{k})$ and $E_2(\mathbf{k})$ is slightly large and the Dirac points move away from the Γ point. In Fig. 7(b), the energy difference between E_1 and E_2 is shown, where the orange region with $E_1 - E_2 < 0.03$ suggests the enhanced anisotropy of the velocity of Dirac cone, e.g., an ellipse with the ratio of major and minor axes being $\simeq 1.2$. Figure 7(c) shows that the tilting angle $\phi (> 0)$ of $E_1(\mathbf{k}) - \mu$ measured from k_x axis has the sign opposite to that of Fig. 2(c). As shown later, such difference in the sign results in the difference of the current direction, i.e., the rotation with respect to the applied electric field. Figure 7(d) shows $E_2(\mathbf{k}) - \mu$ forming a pair of Dirac cone with that of Fig. 7(c), where the deviation of the tilting axis from k_x axis is opposite to that of Fig. 2(d).

Now we examine the electric conductivity. Figure 8 shows conductivity σ_ν , where $\Gamma = 0.0005$. The solid line, (dashed line) denotes σ_x , σ_y , and σ_{xy} (σ_\pm). Note that $\sigma_{xy} < 0$ and has the sign opposite to that of the uni-axial pressure (Fig. 4). The conductivity σ_ν at low temperatures of Fig. 8 is compared with that of Fig. 4. A difference between σ_y and σ_x in the former case is reduced due to hydrostatic pressure, which suppresses an increase of $\sigma_y (> \sigma_x)$ caused by a uniaxial pressure applied along the y direction. Figure 8 also shows the principal value σ_\pm of the conductivity, where $\phi (> 0)$ in the inset denotes an angle between the σ_- axis and the k_x axis. With increasing T , the difference between σ_+ and σ_- increases but is small compared with that of Fig. 4. This comes from a difference at low temperature, where $\sigma_y - \sigma_x$ for the uniaxial pressure is larger than that for

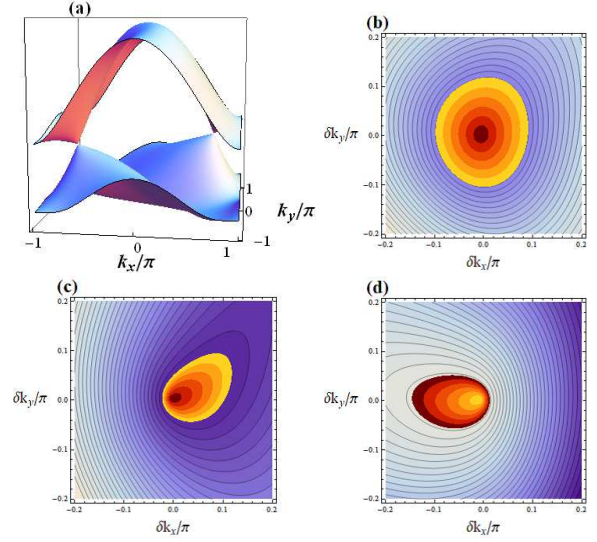


Fig. 7. (Color online) Energy bands of $E_1(\mathbf{k})$ and $E_2(\mathbf{k})$ under hydrostatic pressure, where $\tilde{V}_B = 0.0511$ and $\tilde{V}_C = 0.0032$ for the site potentials. The Dirac points are given by $\mathbf{k}_D = \pm(0.69, 0.44)\pi$. (a) Conduction and valence bands given by $E_1(\mathbf{k})$ (upper band) and $E_2(\mathbf{k})$ (lower band). (b) Magnified scale $E_1(\mathbf{k}) - E_2(\mathbf{k})$ as a function of $\delta\mathbf{k} = \mathbf{k} - \mathbf{k}_D$, where the orange band is given by $|E_1(\mathbf{k}) - E_2(\mathbf{k})| < 0.03$. (c) Conduction band $E_1(\mathbf{k}) - \mu$ as a function of $\delta\mathbf{k}$ with $\mu = 0.172$, where the orange region $0 < E_1(\mathbf{k}) - \mu < 0.005$, (d) Valence band $E_2(\mathbf{k}) - \mu$ as a function of $\delta\mathbf{k}$, where the orange region $-0.005 < E_2(\mathbf{k}) - \mu < 0$.

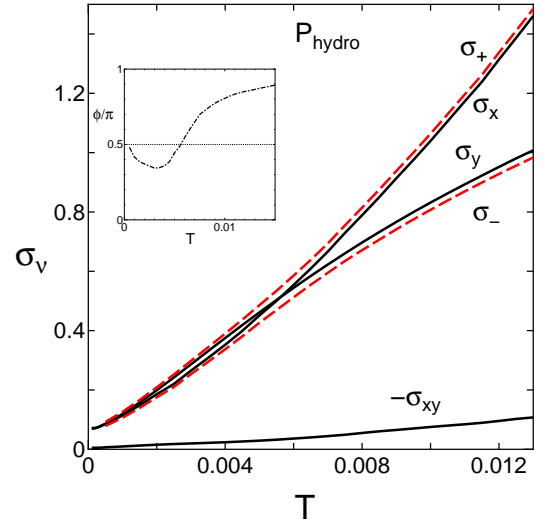


Fig. 8. (Color online) Conductivity σ_ν with $\nu = x, y$ and xy (solid line), and $\nu = \pm$ (dashed line) under hydrostatic pressure. Note that $\sigma_{xy} < 0$ and $\phi/\pi (> 0)$ (the inset) from Eq. (21a).

the hydrostatic pressure. The sign, $\phi > 0$, which is in contrast to that of Fig. 4, is understood from Eq. (21a), since $\sigma_{xy} < 0$ and $\sigma_y > \sigma_x$ in Fig. 8.

Now, we examine the effect of the e-p scattering on the T dependence of conductivity with some choices of R , Eq. (16b), where the effect of the site potential is included in the energy band. Figure 9 shows σ_ν with the fixed $R = 1, 2$, and 3 , in which visible suppression of σ by R is seen compared with that of Fig. 8 ($R = 0$).

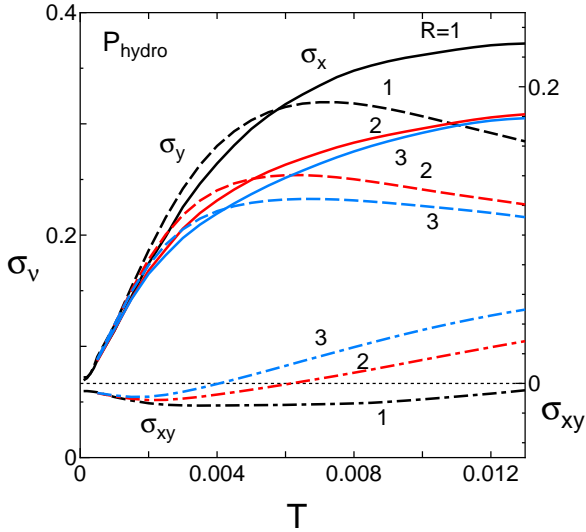


Fig. 9. (Color online) Conductivity σ_ν ($\nu = x, y$, and xy) under hydrostatic pressure in the presence of the e-p interaction with choices of $R = 1, 2$, and 3 .

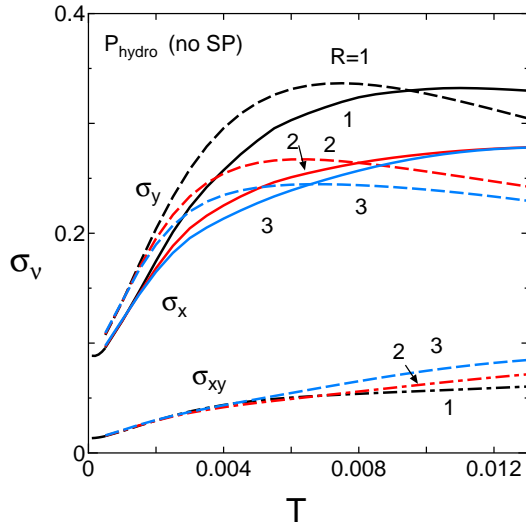


Fig. 10. (Color online) Conductivity σ_ν ($\nu = x, y$ and xy) for hydrostatic pressure with $\tilde{V}_B = \tilde{V}_C = 0$, i.e. no site potential (no SP), which corresponds to Fig. 9.

The crossover temperature, where $\sigma_y > \sigma_x$ at low temperatures and $\sigma_x > \sigma_y$ at high temperatures, decreases with increasing R . The slow increase toward the nearly constant behavior at high T is seen for σ_x while a broad maximum is found for σ_y . σ_{xy} as a function of T takes a minimum and followed by the change of the sign for large R .

Here, to understand the effect of site potentials under hydrostatic pressures, we show the T dependence of σ_ν ($\nu = x, y$, and xy) without site potentials in Fig. 10 and compare with that in Fig. 9. The effect of the variation of $\mu(T)$ on σ_ν is negligibly small, where $\mu(0) = 0.168$. In Fig. 10, the nearly constant behavior is obtained for σ_x with $R = 2$ and 3 . The sign of $\sigma_{xy} (> 0)$ is opposite to that of Fig. 9 at low T . Noting that Fig. 10 resembles

Fig. 5, the sign of σ_{xy} with $+$ ($-$) at low temperatures corresponds to the absence (presence) of interactions. From Figs. 10 and 9, it turns out that the site potentials enhance σ_x but suppress σ_y . The suppression of σ_y is reasonable, since there is alternation of site potentials of V_B and V_C along the y direction on the B-C chain. However, the origin of the enhancement of σ_x is not clear, since the transfer energies b_j in Fig. 1 are complicated for the electron transfer along the x direction.

4. Summary and Discussion

We calculated the T dependence of conductivity σ_ν of Dirac electrons in organic conductor ET under both uniaxial and hydrostatic pressures to examine the nearly constant behaviors at high temperatures. Extending the previous case, where the role of the e-p interaction was examined using the simple two bands of the Dirac cone, we examined the case of ET salts, where the transfer energy of the tight-binding model was obtained from the extended Hückel method and DFT. Such a model provides anomalous T dependence of conductivity due to the tilted Dirac cone. With a moderate choice of the e-p interaction, our result suggests the almost constant conductivity at high temperature. The presence of the off-diagonal component (σ_{xy}), which is associated with the deviation of the tilting axis of the Dirac cone from the k_x or k_y axis, results in the principal axis with clockwise or anticlockwise rotation depending on the sign of σ_{xy} . Within the mean-field theory, we examined the effect of interactions on the conductivity with the tilted Dirac cone. Compared with σ_ν without interactions, σ_x is enhanced but σ_y is suppressed.

Here, we note on the role of the e-p interaction²⁷⁾ in the nodal line semimetal, $[\text{Pd}(\text{dddt})_2]$, which also exhibits similar resistivity at high T .¹⁹⁾ Although the system differs due to a line of Dirac points in 3D momentum space, electrons close to the nodal line show rather robust 2D DOS. Taking a moderate magnitude of the e-p coupling constant, the almost T independent conductivity in the 2D plane has been obtained.³⁵⁾

Finally, we compare our result with that of experiment. Temperature dependence of resistance (corresponding to the inverse of the conductivity) under hydrostatic pressures shows nearly constant behavior at high temperatures and a minimum at low temperatures, while the minimum is invisible for uniaxial pressure.²⁾ Our results show the broad maximum for σ_y and monotonic variation for σ_x . Although we obtain the qualitative coincidence, the detail correspondence between them e.g., the direction of measurement is needed for the quantitative comparison. It also remains a future problem to clarify if the conductivity under pressure suggests the presence of interaction. The validity of our present calculation may be examined by the measurement of the deviation angle of the principal axis, i.e., the clockwise (anticlockwise) for the case without interaction (with interaction).

Acknowledgements

We thank R. Kato for useful discussions on the effect of the e-p interaction.

- 1) K. S. Novoselov, A. K. Geim, S. V. Morozov, D. Jiang, M. I. Katsnelson, I. V. Grigorieva, S. V. Dubonos, and A. A. Firsov, *Nature* **438**, 197 (2005).
- 2) K. Kajita, Y. Nishio, N. Tajima, Y. Suzumura, and A. Kobayashi, *J. Phys. Soc. Jpn.* **83**, 072002 (2014).
- 3) T. Mori, A. Kobayashi, Y. Sasaki, H. Kobayashi, G. Saito, and H. Inokuchi, *Chem. Lett.* **13**, 957 (1984).
- 4) A. Kobayashi, S. Katayama, K. Noguchi, and Y. Suzumura, *J. Phys. Soc. Jpn.* **73**, (2004) 3135 (2004).
- 5) S. Katayama, A. Kobayashi, and Y. Suzumura, *J. Phys. Soc. Jpn.* **75**, 054705 (2006).
- 6) R. Kondo, S. Kagoshima, and J. Harada, *Rev. Sci. Instrum.* **76**, 093902 (2005).
- 7) H. Kino and T. Miyazaki, *J. Phys. Soc. Jpn.* **75**, 034704 (2006).
- 8) S. Katayama, A. Kobayashi, and Y. Suzumura, *Eur. Phys. J. B* **67**, 139 (2009).
- 9) M. Inokuchi, H. Tajima, A. Kobayashi, H. Kuroda, R. Kato, T. Naito, and H. Kobayashi, *Synth. Met.* **56**, 2495 (1993).
- 10) M. Inokuchi, H. Tajima, A. Kobayashi, T. Ohta, H. Kuroda, R. Kato, T. Naito, and H. Kobayashi, *Bull. Chem. Soc. Jpn.* **68**, 547 (1995).
- 11) R. Kondo, S. Kagoshima, N. Tajima, and R. Kato, *J. Phys. Soc. Jpn.* **78**, 114714 (2009).
- 12) T. Morinari, and Y. Suzumura, *J. Phys. Soc. Jpn.* **83**, 094701 (2014).
- 13) T. Naito, R. Doi, and Y. Suzumura, *J. Phys. Soc. Jpn.* **89**, 023701 (2020).
- 14) K. Kajita, T. Ojio, H. Fujii, Y. Nishio, H. Kobayashi, A. Kobayashi, and R. Kato, *J. Phys. Soc. Jpn.* **61**, 23 (1992).
- 15) N. Tajima, M. Tamura, Y. Nishio, K. Kajita, and Y. Iye, *J. Phys. Soc. Jpn.* **69**, 543 (2000).
- 16) N. Tajima, A. Ebina-Tajima, M. Tamura, Y. Nishio, and K. Kajita, *J. Phys. Soc. Jpn.* **71**, 1832 (2002).
- 17) N. Tajima, S. Sugawara, M. Tamura, R. Kato, Y. Nishio, and K. Kajita, *EPL* **80**, 47002 (2007).
- 18) D. Liu, K. Ishikawa, R. Takehara, K. Miyagawa, M. Tanuma, and K. Kanoda, *Phys. Rev. Lett.* **116**, 226401 (2016).
- 19) R. Kato, H. Cui, T. Tsumuraya, T. Miyazaki, and Y. Suzumura, *J. Am. Chem. Soc.* **139**, 1770 (2017).
- 20) R. Kato and Y. Suzumura, *J. Phys. Soc. Jpn.* **86**, 064705 (2017).
- 21) Y. Suzumura, H.B. Cui, and R. Kato, *J. Phys. Soc. Jpn.* **87**, 084702 (2018),
- 22) B. Zhou, S. Ishibashi, T. Ishii, T. Sekine, R. Tkehara, K. Miyagawa, K. Kanoda, E. Nishibori, and A. Kobayashi, *Chem. Commun.* **55**, 3327 (2019).
- 23) R. Kato and Y. Suzumura, *J. Phys. Soc. Jpn.* **89**, 044713 (2020).
- 24) N. H. Shon and T. Ando, *J. Phys. Soc. Jpn.* **67**, 2421 (1998).
- 25) Y. Suzumura, I. Igor, and M. Ogata *J. Phys. Soc. Jpn.* **83**, 023701 (2014).
- 26) N.M.R. Peres, F. Guinea, and A.H. Castro Neto, *Phys. Rev. B* **83**, 125411 (2006).
- 27) Y. Suzumura, and M. Ogata *Phys. Rev. B* **87**, 093704 (2018).
- 28) A. Kobayashi, S. Katayama, Y. Suzumura, and H. Fukuyama, *J. Phys. Soc. Jpn.* **76** 034711 (2007).
- 29) M. O. Goerbig, J.-N. Fuchs, G. Montambaux, and F. Piéchon, *Phys. Rev. B* **78**, 045415 (2008).
- 30) A. Kobayashi, Y. Suzumura, and H. Fukuyama, *J. Phys. Soc. Jpn.* **77**, 064718 (2008).
- 31) H. Fröhlich, *Proc. Phys. Soc. A* **223**, 296 (1954).
- 32) T. Holstein, *Ann. Phys.* **29**, 410 (1964).
- 33) A.A. Abrikosov, L.P. Gorkov, and I.E. Dzyaloshinskii, *Methods of Quantum Field Theory in Statistical Physics*, (Prentice-Hall, Englewood Cliffs, N.J. 1963).
- 34) S. Katayama, A. Kobayashi, and Y. Suzumura, *J. Phys. Soc. Jpn.* **75**, 023708 (2006).
- 35) Y. Suzumura, R. Kato, and M. Ogata, *Crystals*, **2020**, 10, 862.